Supporting Information

Resolving the conductivity puzzle of halogen-doped $Li_7P_3S_{11}$ solid electrolyte: atomistic insights from Li and polyhedral dynamics

Seung-Won Yoo[1], David O. Scanlon[2], Hee Jung Park[1,3] and Yong-Seok Choi[1,*]

[1] Department of Materials Science and Engineering, Dankook University, 119 Dandae-ro, Cheonan 31116, South Korea

[2] The School of Chemistry, University of Birmingham, Edgbaston, Birmingham, UK

[3] Hydrogen research center, Dankook University, 119 Dandae-ro, Dongnam-gu, Cheonan, 31116, Republic of Korea

*To whom correspondence should be addressed. Yong-Seok Choi (yschoi@dankook.ac.kr)

Table of contents

List of Figures

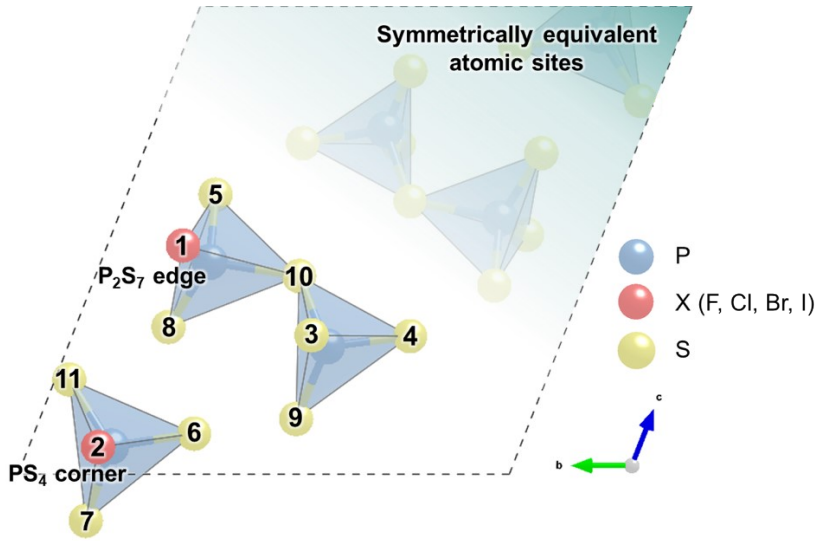

Figure S1. Unit cell structure of the $Li_7P_3S_{11}$ (LPS) solid electrolyte. Blue and yellow spheres represent phosphorus (P) and sulfur (S) atoms, respectively. Red spheres indicate the sites (index numbers) where halogen elements (F, Cl, Br, I) are doped in this study. The LPS structure contains a total of eleven crystallographically distinct sulfur atoms. The sulfur sites that are potentially available for halogen doping are labeled with numbers. The faint atoms shown in the upper right portion of the figure represent symmetry-equivalent positions. Of all sulfur sites in LPS, edge sites of P2S7 is found to be the most preferential sites which is also confirmed from Madelung potential analysis (see Figure S17).

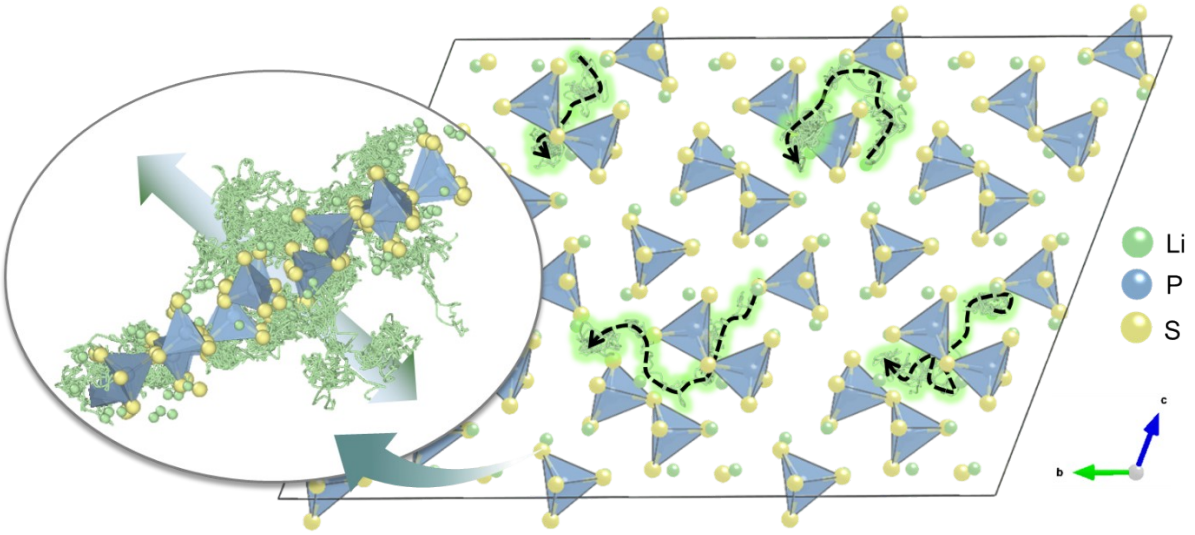

Figure S2. Molecular dynamics (MD) simulation results showing the diffusion pathways (light green trajectories) of Li ions within the LPS supercell. Blue, yellow, and light green spheres represent phosphorus (P), sulfur (S), and lithium (Li) atoms, respectively. The magnified view in the left inset clearly exhibit the migration of Li ions through P_2S_7 polyhedra, which causes the transformation from P_2S_7 into other substructures.

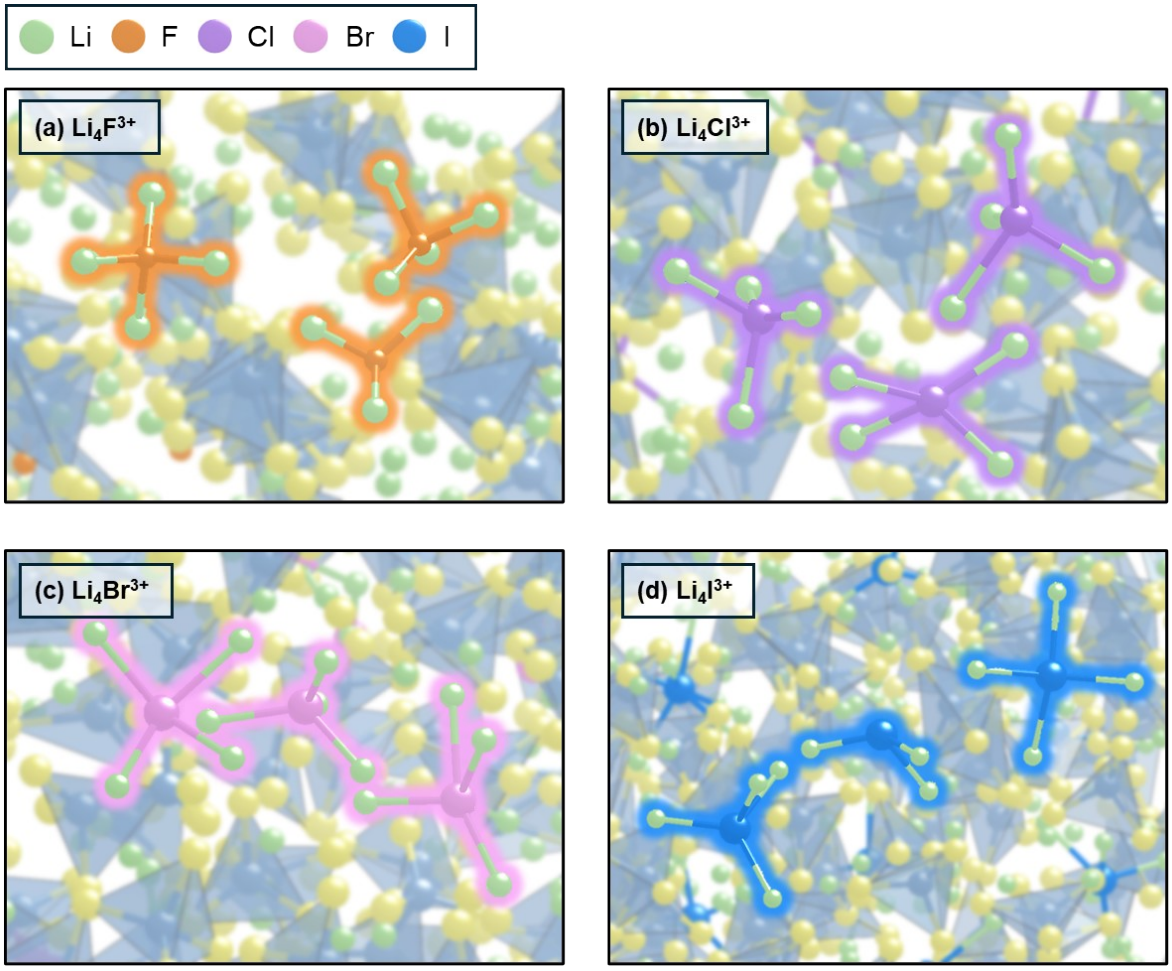

Figure S3. Formation of Li_4X^{3+} complexes during molecular dynamics (MD) simulations of X-doped LPS (X = F, Cl, Br, I). Each panel shows a transiently formed Li_4X^{3+} structure observed during the simulation for the halogen-doped models: (a) Li_4F^{3+}, (b) Li_4Cl^{3+}, (c) Li_4Br^{3+}, and (d) Li_4I^{3+}. In certain segments of the simulation trajectories, halide ions were observed to dissociate from PS_xX polyhedral units and interact with nearby Li ions to form localized complexes. Green, yellow, and blue spheres represent lithium (Li), sulfur (S), and phosphorus (P) atoms, respectively, while orange, purple, pink, and light blue spheres correspond to fluorine (F), chlorine (Cl), bromine (Br), and iodine (I), respectively.

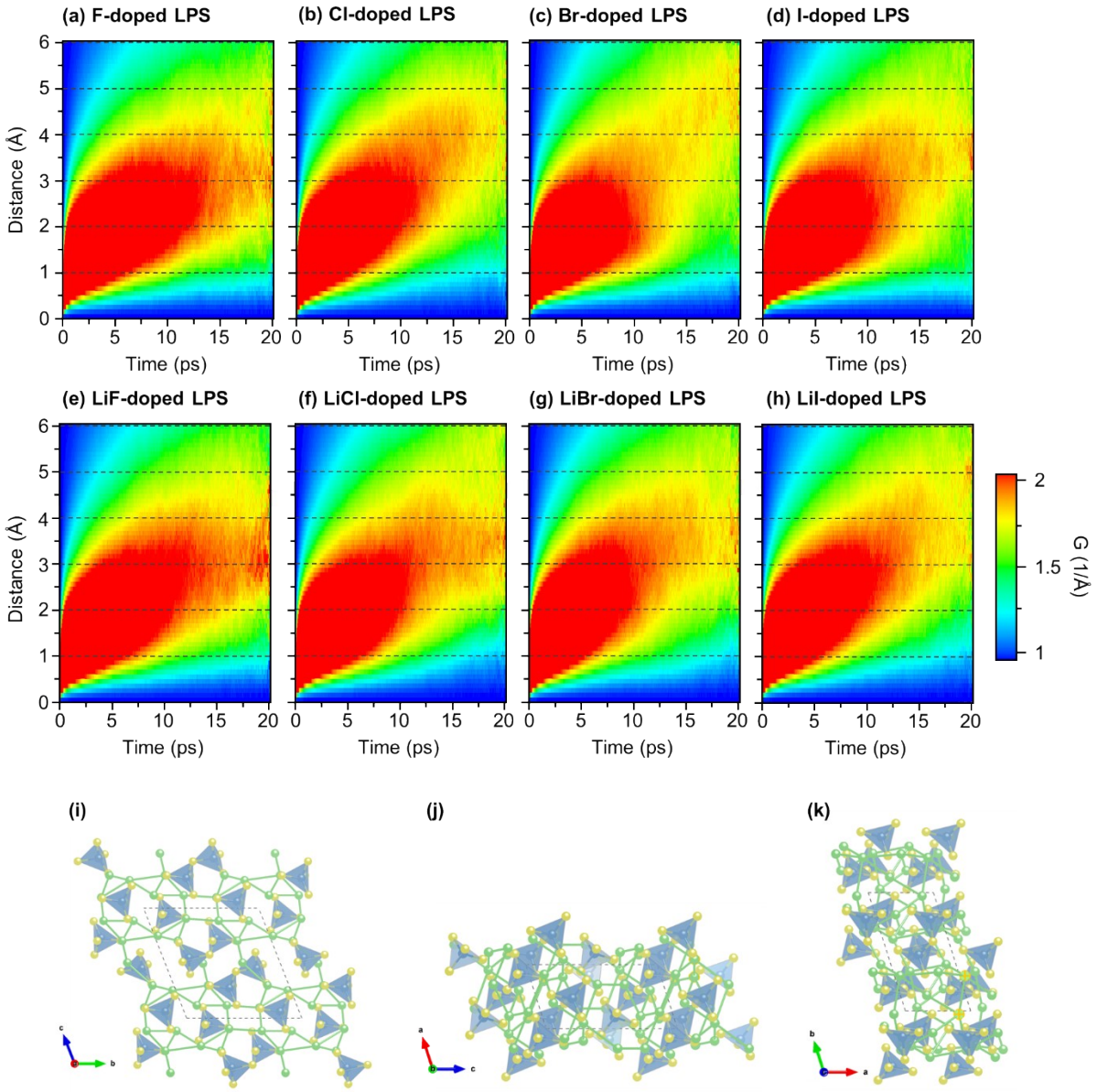

Figure S4. Van Hove functions representing the diffusion distance of Li ions in LPS solid electrolyte. Panels (a) - (d) show the results for systems where halogen elements (F, Cl, Br, I) are doped at S sites of PS_x polyhedra, while panels (e) - (h) correspond to cases where LiX (X = F, Cl, Br, I) species are doped into the LPS structure. The representative Li diffusion behavior in each system in visualized through the color distribution over simulation time. Possible diffusion pathways within 4 Å, corresponding to the maximum Li^+ hopping distance in the LPS structure shown in (a)–(h), are visualized along the (i) a-axis, (j) b-axis, and (k) c-axis.

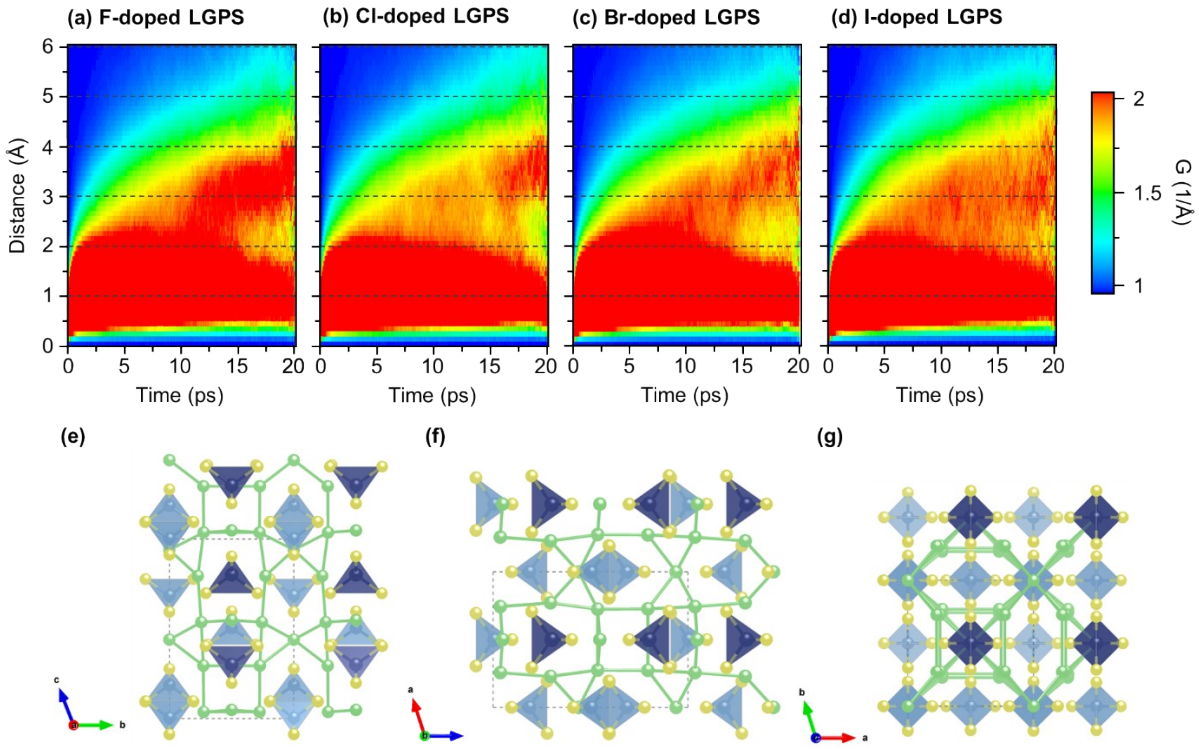

Figure S5. Van Hove functions representing the diffusion distance of Li ions in LPS solid electrolyte. Panels (a) - (d) show the results for systems where halogen elements (F, Cl, Br, I) are doped at S sites of GeS_4 tetrahedra in the LGPS structure. The representative Li diffusion behavior in each system in visualized through the color distribution over simulation time. Possible diffusion pathways within 4 Å, corresponding to the maximum Li^+ hopping distance in the LGPS structure shown in (a)–(d), are visualized along the (e) a-axis, (f) b-axis, and (g) c-axis.

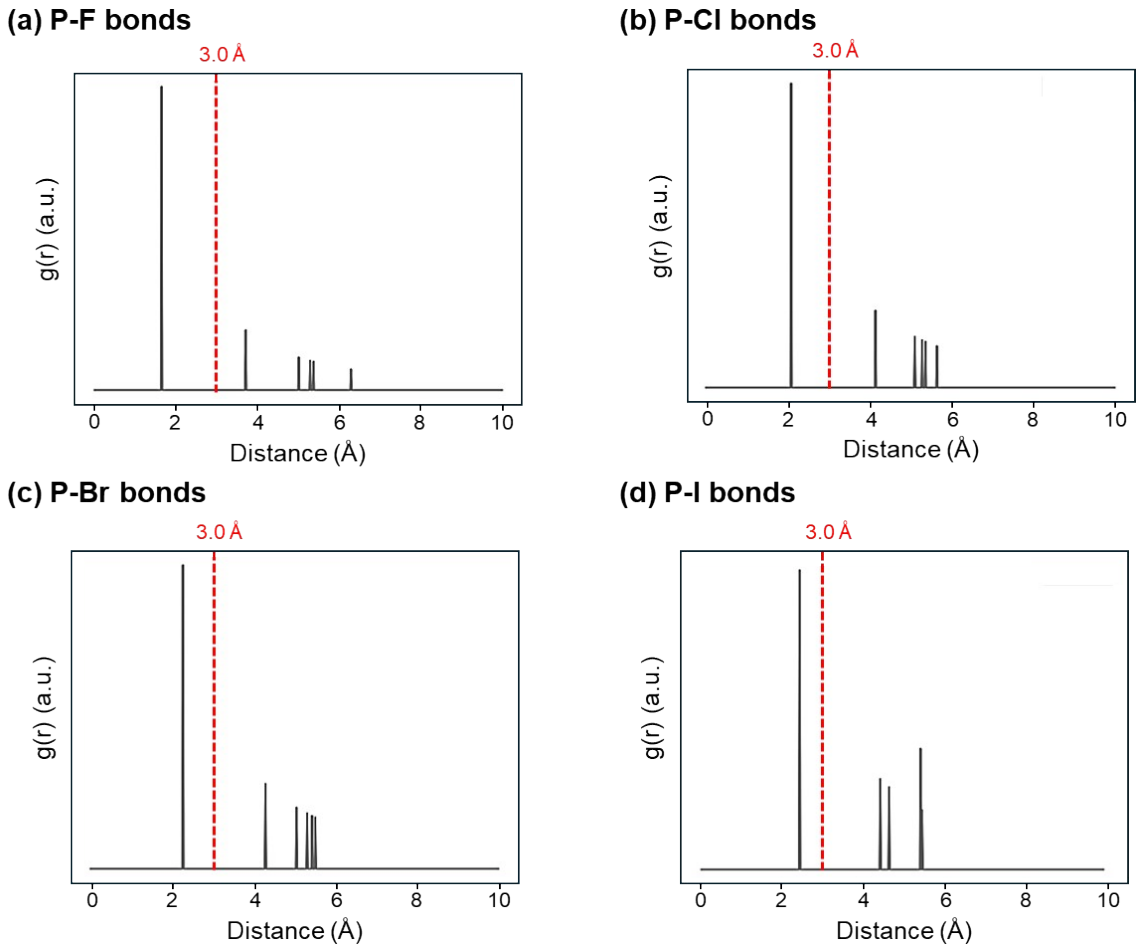

Figure S6. Radial distribution functions (RDF) plotted for (a) P–F bonds of F-doped LPS, (b) P–Cl bonds of Cl-doped LPS, (c) P–Br bonds of Br-doped LPS, and (d) P–I bonds of I-doped LPS. Vertical red dashed lines indicate the cutoff distance of 3.0 Å.

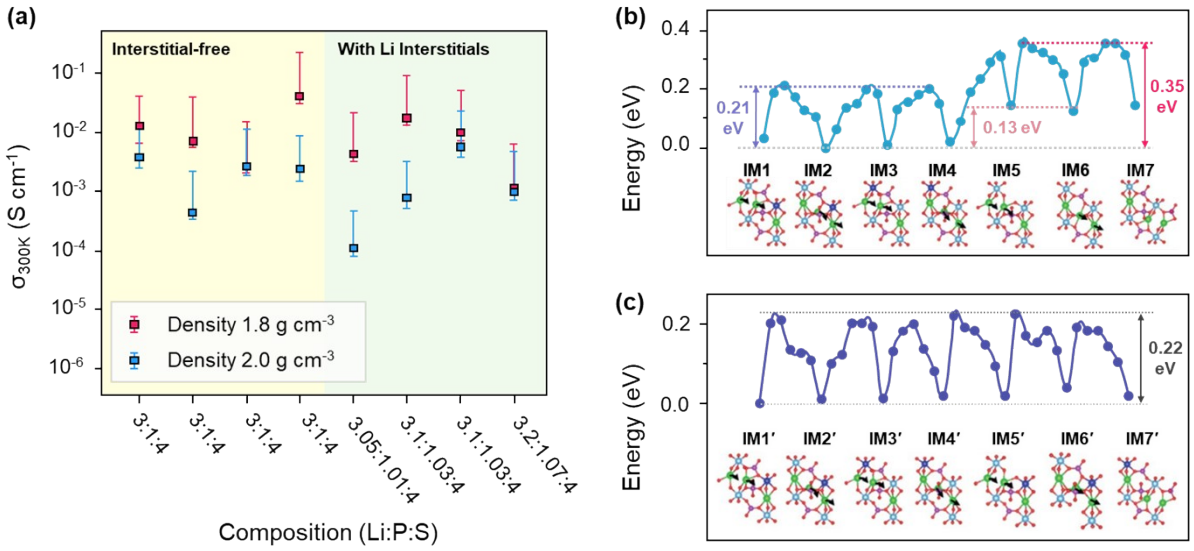

Figure S7. (a) Ionic conductivity of amorphous Li_3PS_4 solid electrolytes at 300 K obtained by extrapolation of Arrhenius plots calculated at five to seven different temperatures. (b) and (c) Energy profiles of the cooperative Li-ion migration pathways in LATP solid electrolytes, together with schematic illustrations of the intermediate configurations shown as insets. Panel (a) is reproduced from Ref. [1],and panels (b) and (c) are reproduced from Ref. [2]. In amorphous sulfide electrolytes such as Li_3PS_4, increasing Li content does not necessarily enhance ionic conductivity; instead, Li-rich compositions can exhibit slightly reduced conductivity, suggesting that additional Li may induce local dynamic disorder or "rattling" behavior in structurally flexible frameworks. In contrast, crystalline oxide electrolytes with rigid frameworks (e.g., LATP) support cooperative Li-ion migration along well-defined pathways, where additional Li can participate constructively in the migration mechanism.

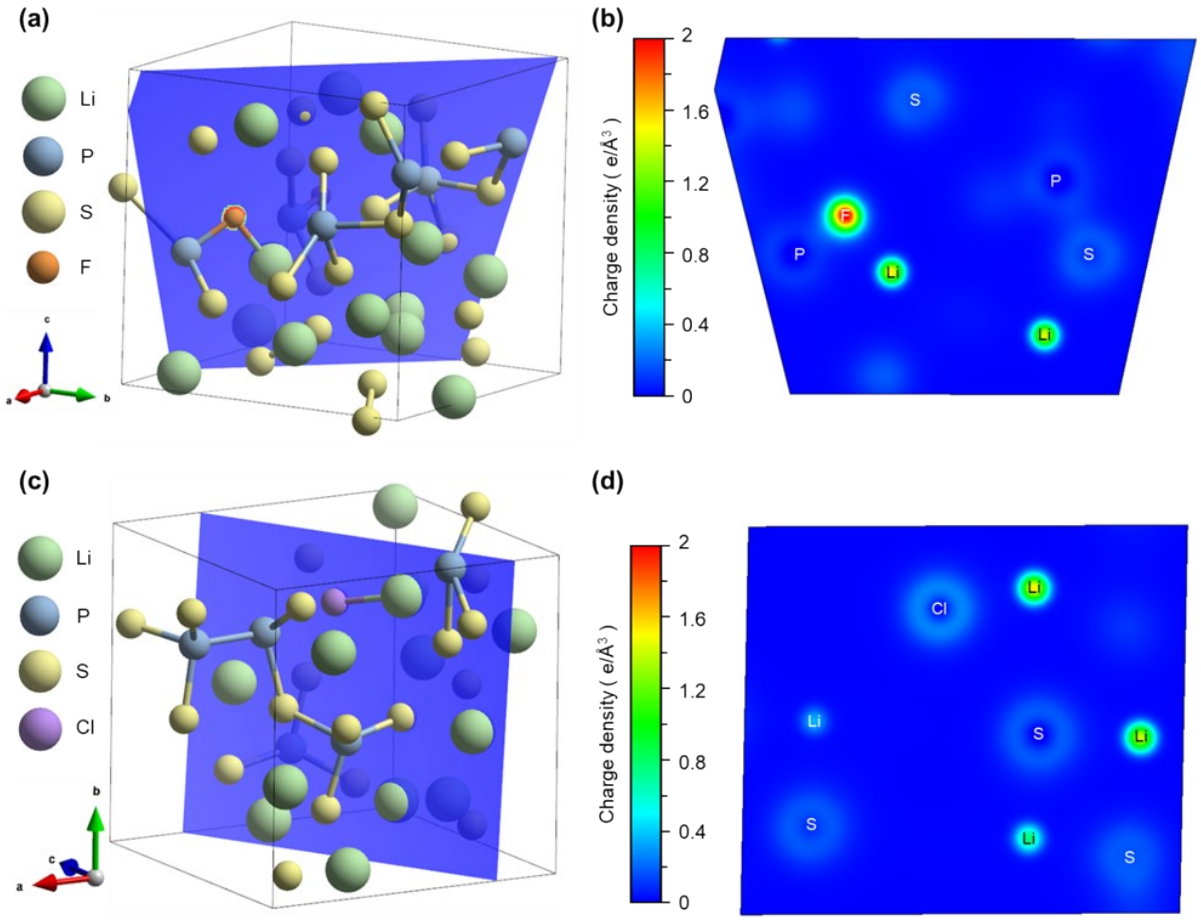

Figure S8. Structural cross-sections and corresponding charge density maps of F- and Cl-doped LPS. Atomic structure of (a) F- and (c) Cl-doped LPS showing the selected crystallographic plane used for charge density analysis. Two-dimensional charge density distribution of (b) F- and (d) Cl-doped LPS on the planes denoted in (a) and (c), respectively. A strong and highly localized charge accumulation is observed around the F site, reflecting its high electronegativity and strong Li–F interaction. Compared to F, the charge distribution around Cl is more diffuse and less localized. The contrast between (b) and (d) indicates that the Li–F interaction is significantly stronger than the Li–Cl interaction, suggesting that strong electrostatic localization in the F-doped system can hinder Li^+ migration despite substantial polyhedral transformation.

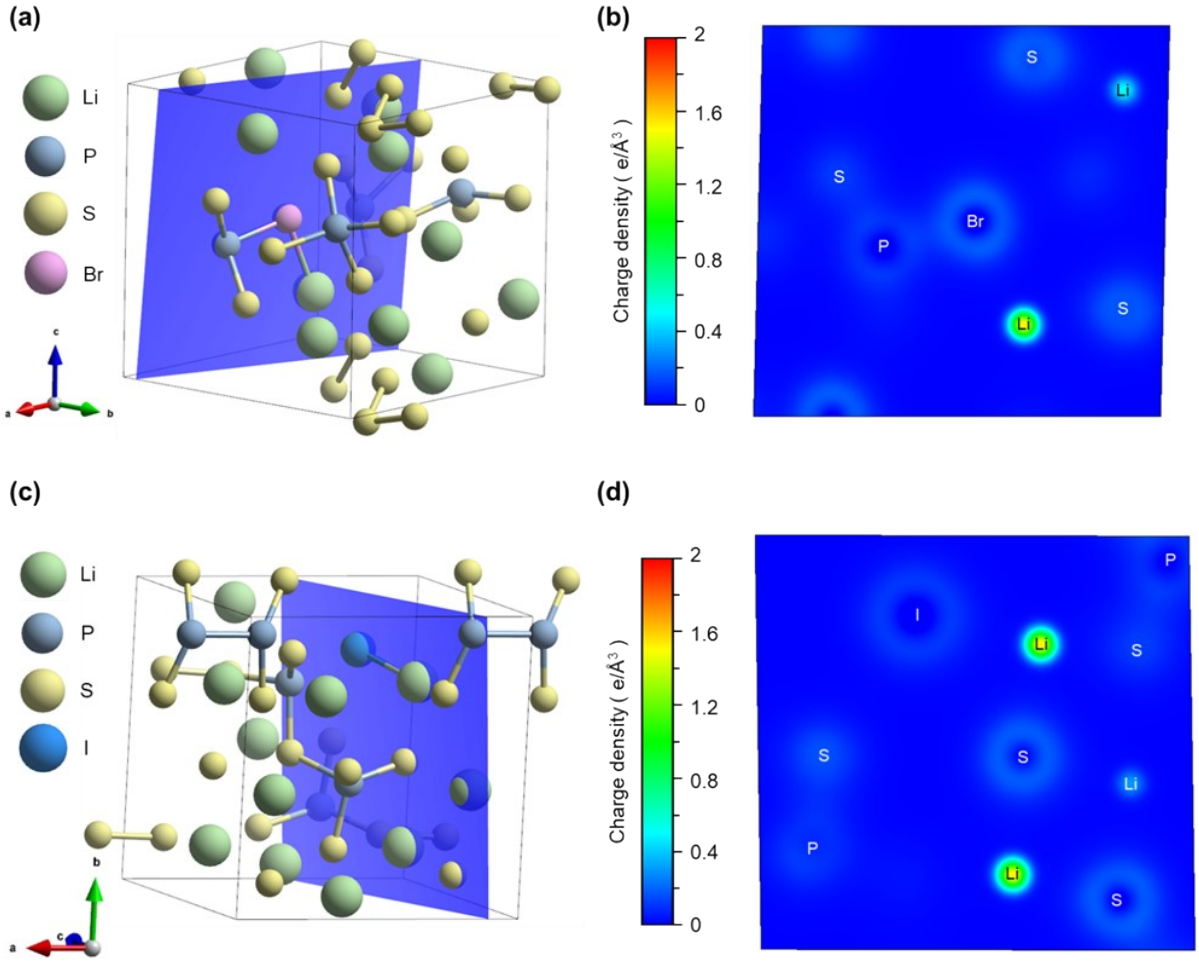

Figure S9. Structural cross-sections and corresponding charge density maps of Br- and I-doped LPS. Atomic structure of (a) Br- and (c) I-doped LPS with the selected crystallographic plane. Two-dimensional charge density distribution of (b) Br- and (d) I-doped LPS on the planes denoted in (a) and (c), respectively. The charge density around the halogen site becomes progressively less localized from Br to I, consistent with decreasing electronegativity and weaker Li–X interactions. This systematic reduction in charge localization from F to I (Figures S8–S9) provides electronic-structure-level evidence that strong Li–F interaction can create locally confined electrostatic environments that impede Li^+ transport.

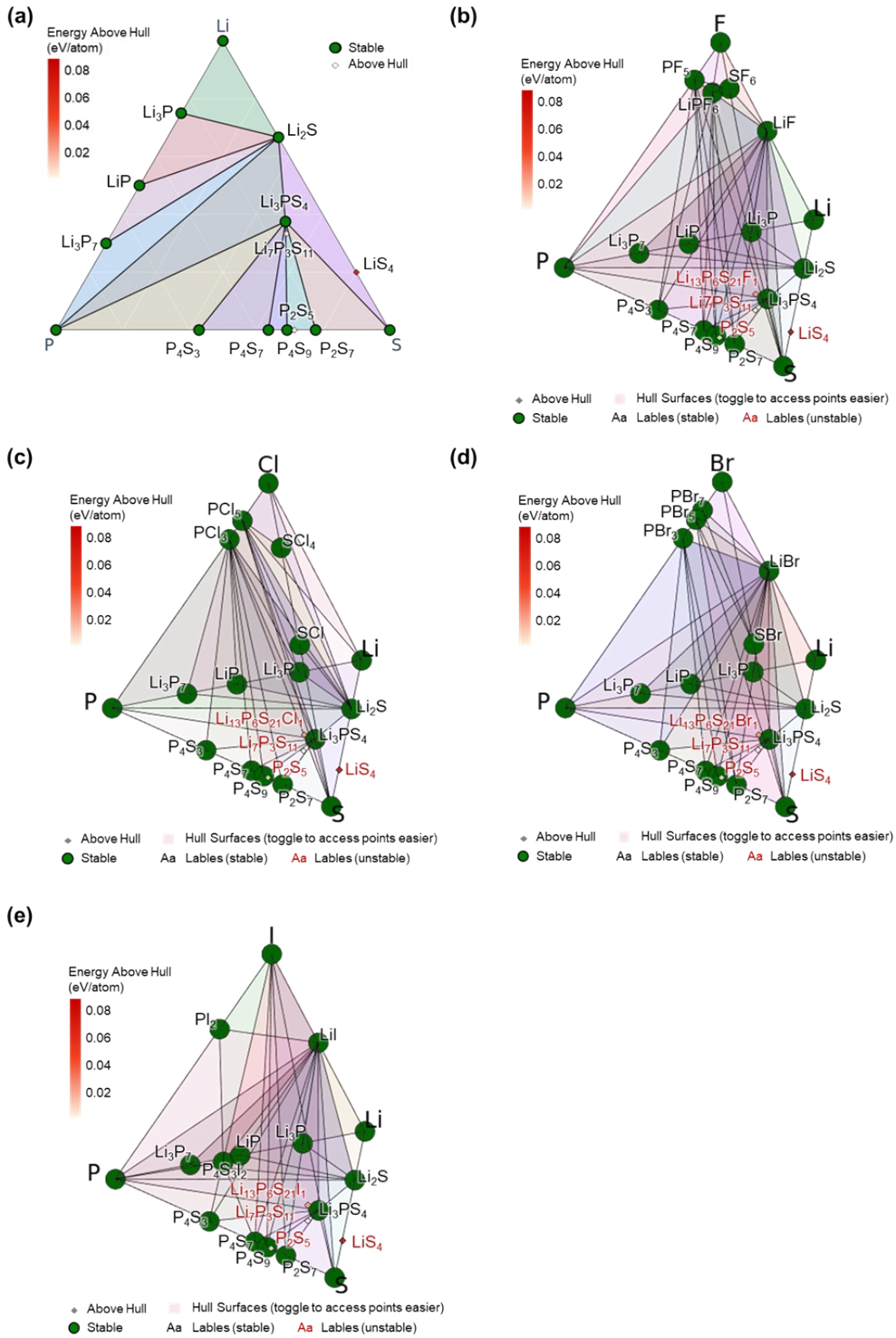

Figure S10. DFT-calculated convex-hull phase diagrams used for thermodynamic stability analysis of $Li_7P_3S_{11}$ (LPS) and halogen-doped systems. (a) Li–P–S ternary phase diagram for

pristine LPS. (b–e) Quaternary phase diagrams for (b) Li–P–S–F, (c) Li–P–S–Cl, (d) Li–P–S–Br, and (e) Li–P–S–I systems constructed from total DFT energies. Stable phases located on the convex hull are indicated in green, while unstable phases are colored according to their energy above hull (eV/atom).

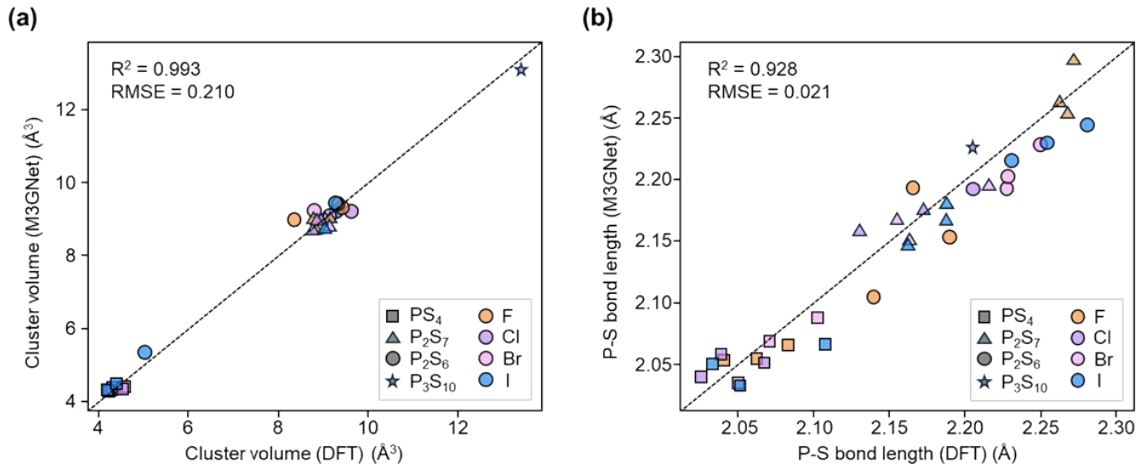

Figure S11. Parity plots comparing the (a) cluster volume and (b) P–X bond lengths of halogen-doped $Li_7P_3S_{11}$ structures optimized using density functional theory (DFT) and the M3GNet interatomic potential. The halogen-doped $Li_7P_3S_{11}$ structures were obtained from the snapshots of ML-MD simulations. The performance metrics of root mean square error (RMSE) and regression coefficient (R^2) are indicated on the graph. The dashed line indicates perfect agreement between the two methods. The strong linear correlation between the DFT and M3GNet results demonstrate that the M3GNet potential accurately reproduces the DFT-level structural features of the LPS system, indicating its reliability for performing simulations at near-DFT accuracy.

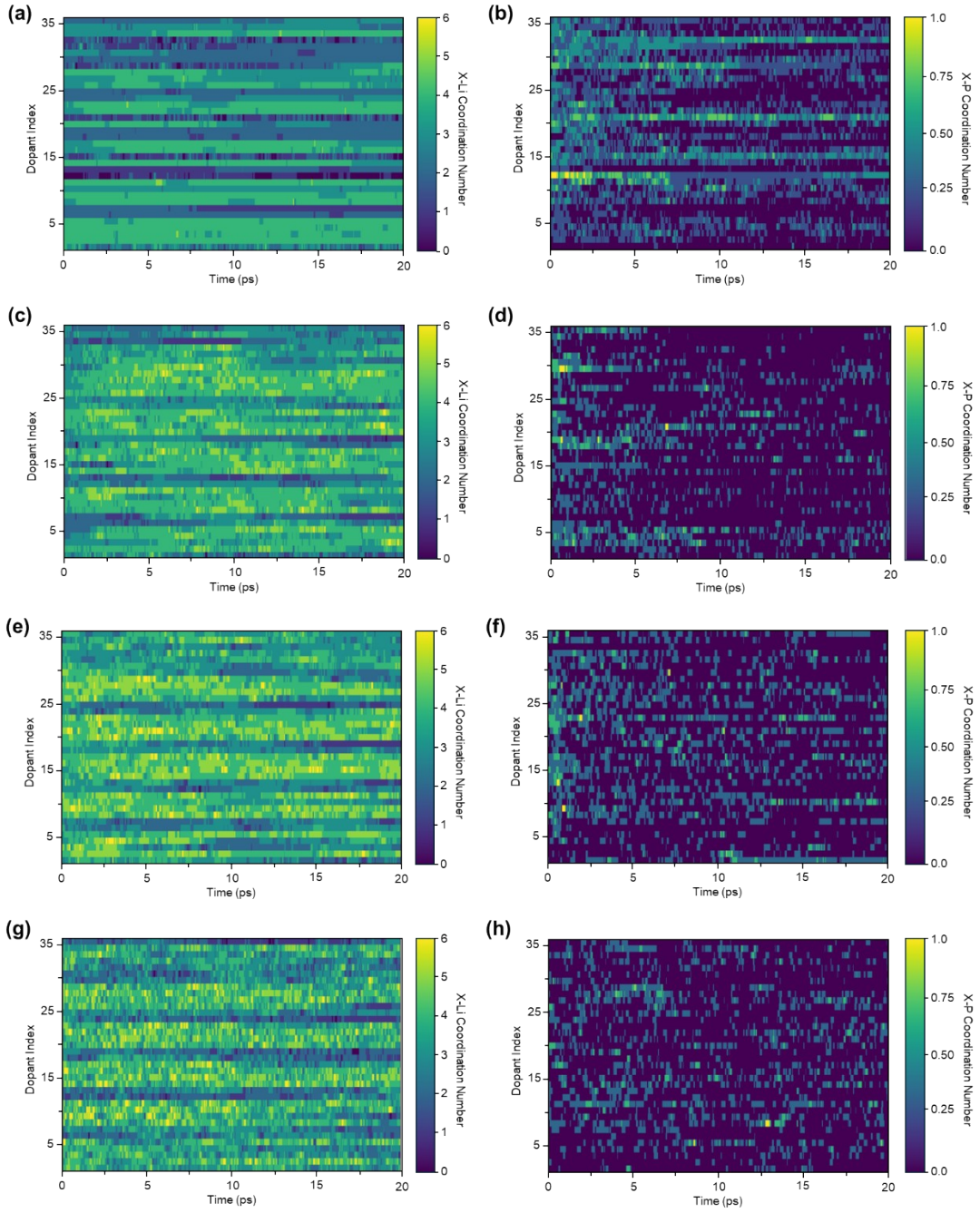

Figure S12. Time-resolved coordination number heatmaps of halogen dopants in $Li_7P_3S_{11}$ obtained from ML-MD simulations. Panels (a), (c), (e), and (g) show the dopant–Li coordination numbers for F-, Cl-, Br-, and I-doped LPS, respectively, while panels (b), (d), (f), and (h) show the corresponding dopant–P coordination numbers. The horizontal axis represents the simulation time (ps) over the 20 ps ML-MD trajectory, and the vertical axis represents the

index of individual dopant atoms in the simulation cell. The color scale indicates the instantaneous coordination number at each time step. The Li–X bonds are repeatedly broken and reformed during the 20 ps molecular dynamics simulations. This behavior indicates that, even within a relatively short simulation time, the doped halogen ions dynamically interact with Li, thereby influencing ionic conductivity. In particular, for the F dopant, the Li–X bonds are less frequently broken compared to those with other halogen dopants. This can be attributed to the high electronegativity of F, which leads to stronger Li–F interactions and consequently acts as a factor that suppresses Li diffusion. On the other hand, for the coordination between halogen dopants and P, the coordination values fluctuate between 0 and 1 during the 20 ps molecular dynamics simulations. This behavior indirectly suggests that the halogen dopants form and dissociate bonds with P, leading to the formation of various PS_x structural units.

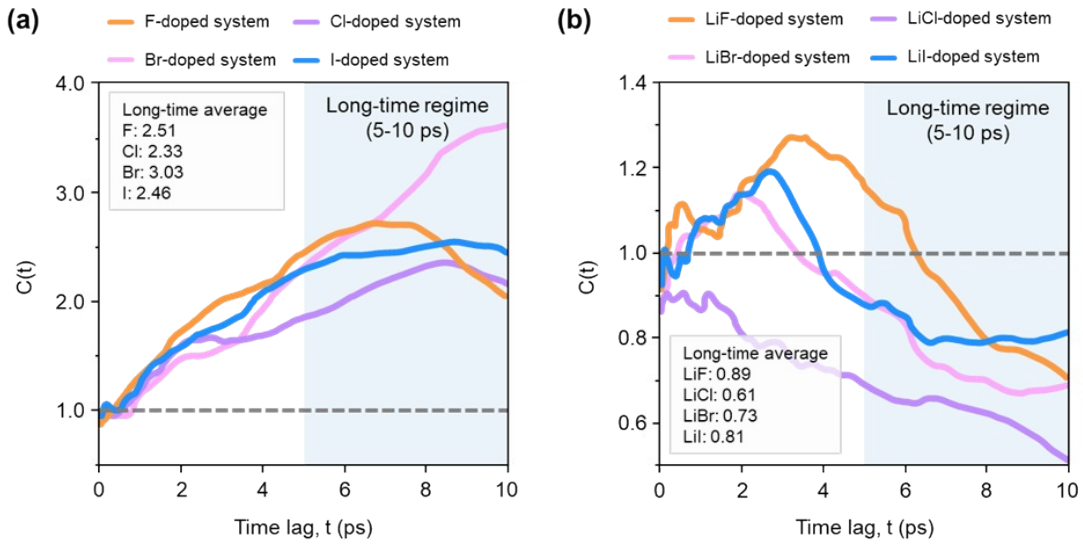

Figure S13. Cooperative motion metric $C(t)$ for Li-ion dynamics in halogen-doped (X-doped) and lithium-halide-doped (LiX-doped) $Li_7P_3S_{11}$ (LPS) structures obtained from ML-MD trajectories. The shaded region (5–10 ps) represents the long-time regime used to evaluate the degree of correlated ionic motion, and the reported values correspond to the averaged $C(t)$within this interval. The dashed horizontal line indicates $C(t) = 1$, which separates anticorrelated $(C(t) > 1)$and correlated $(C(t) < 1)$ionic motion. The X-doped LPS systems exhibit weaker or anticorrelated Li-ion motion with $C(t) > 1$, whereas the LiX-doped systems show enhanced collective motion $(C(t) \lesssim 1)$.

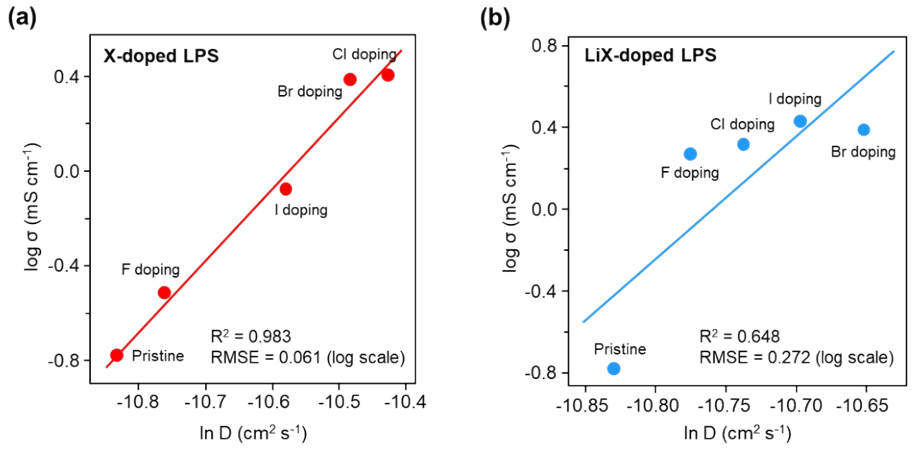

Figure S14. Parity plots of (a) X-doped LPS and (b) LiX-doped LPS comparing the calculated lithium-ion diffusivity (D) obtained from ML-MD simulations with the experimentally reported ionic conductivity (σ) of $Li_7P_3S_{11}$-based solid electrolytes collected from the literature. The dashed lines represent linear regression fits, and the corresponding R^2 and RMSE values are indicated. Although the simulations systematically overestimate the absolute ionic conductivity due to the absence of microstructural effects such as grain boundaries, defects, and secondary phases, the model structures with halogen dopants in P_2S_7 motifs successfully reproduce the relative trends, demonstrating the preference of halogen dopants in P_2S_7 motifs rather than in PS_4 motifs.

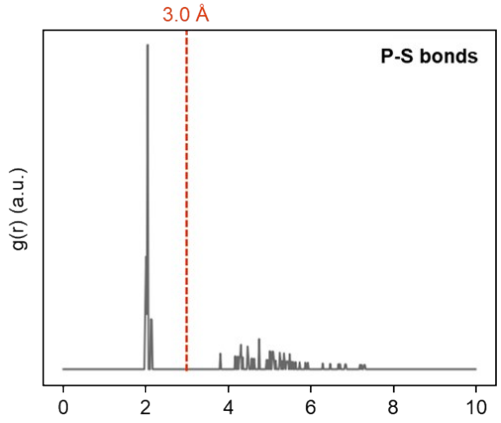

Figure S15. Radial distribution function (RDF) of P–S atomic pairs in $Li_7P_3S_{11}$ obtained from molecular dynamics simulations. The RDF shows a pronounced first peak at approximately 2.0–2.2 Å, corresponding to the typical P–S covalent bond lengths reported for Li–P–S systems (terminal ~1.9 Å and bridging ~2.1 Å). To robustly identify chemically meaningful P–S bonds under thermal fluctuations during MD simulations, a bond cutoff distance of 3.0 Å was adopted, as indicated by the red dashed line. This cutoff fully includes the first coordination shell while remaining clearly separated from the second coordination shell, thereby enabling stable tracking of P–S bonds for evaluating PS_x polyhedral transformations.

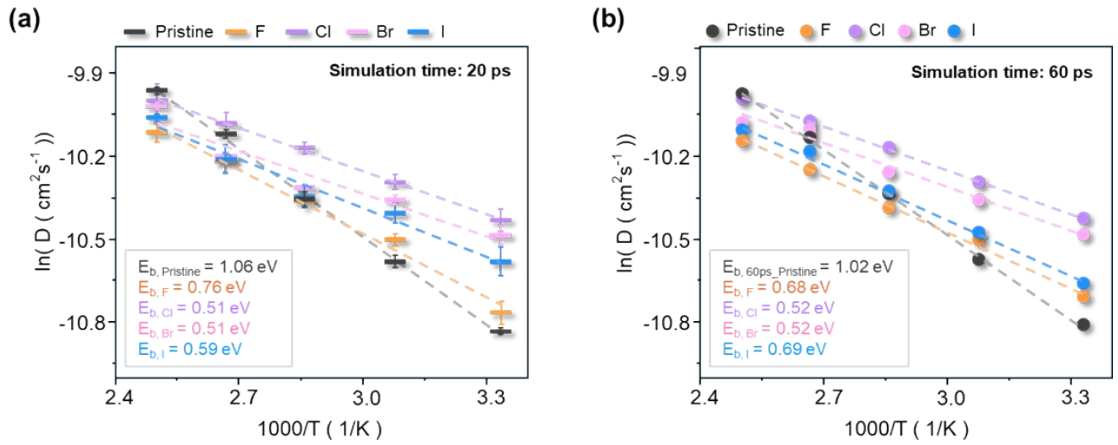

Figure S16. Arrhenius plots of Li-ion diffusivity in halogen-doped $Li_7P_3S_{11}$ (LPS) solid electrolytes obtained from AIMD simulations at temperatures ranging from 300 to 400 K. The diffusivity values are plotted in logarithmic scale as a function of inverse temperature for pristine and X-doped systems (X = F, Cl, Br, I). (a) Results obtained from 20 ps AIMD simulations and (b) results from 60 ps simulations. The similar diffusivity trends observed for different dopants in both cases indicate that a 20 ps simulation time is sufficient to reliably capture the relative changes in Li-ion transport behavior induced by halogen doping. Activation energies extracted from the Arrhenius fits are shown in each panel.

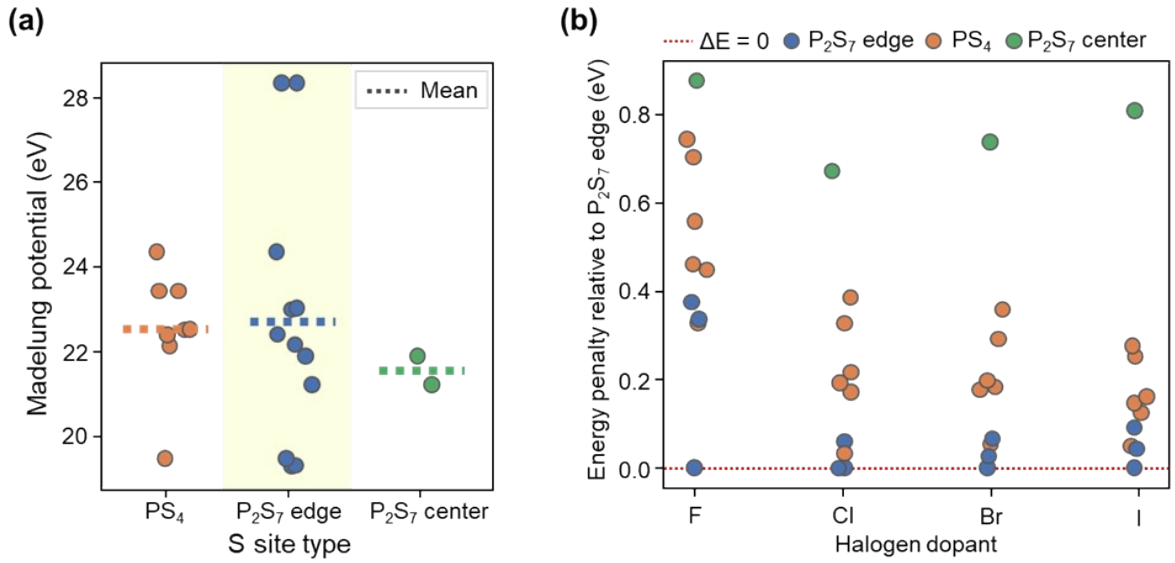

Figure S17. Site preference analysis for halogen dopants in $Li_7P_3S_{11}$ (LPS). (a) Comparison of Madelung potentials for different sulfur sites in the LPS structure, where the y-axis represents the Madelung potential (eV) and dashed lines indicate the average values for each site type. (b) Relative energy penalty with respect to the P_2S_7 edge site for halogen substitution (X = F, Cl, Br, I) calculated using DFT. Madelung potential [3] is the electrostatic potential of an ion in a crystal by summing up the charges of adjacent ions, which has been used as a key descriptor for explaining the phenomenon arising from point defects [4,5]. S ions with lower Madelung potentials have more unstable valence electrons [5] and thus, can be readily replaced by halogen dopants. When examining the calculated Madelung potentials (Figure S17a), S in the edge of P2S7 shows the lowest value among the other sites, suggesting the high site preference of halogen dopants on P2S7 edge. Such strong preference can also be observed in the relative energy penalty calculated for X-doped LPS with differing dopant sites (Figure S17b).

Additional Notes

Effect of Li interstitial on the ionic conductivity of solid electrolytes with rattling behavior

Previous studies on amorphous sulfide electrolytes have reported that increasing Li content does not always lead to improved ionic conductivity. For example, in amorphous Li_3PS_4 systems with different PS_x polyhedral configurations, Li-rich compositions exhibited slightly reduced ionic conductivity compared with stoichiometric compositions, suggesting that excessive Li can introduce dynamic disorder in structurally flexible sulfide frameworks (Figure S7a). In such systems, frequent polyhedral rearrangements may promote local Li vibrational motion rather than long-range ion transport.

In contrast, crystalline oxide electrolytes with rigid frameworks often show the opposite behavior. For instance, in NASICON-type LATP electrolytes, cooperative Li-ion migration occurs along well-defined diffusion pathways within the stable framework, and additional Li ions can participate in these cooperative mechanisms, facilitating Li transport (Figures S7b and S7c). These contrasting examples highlight that the effect of additional Li strongly depends on the structural dynamics of the host lattice. Because LPS exhibits pronounced polyhedral distortions and structural rearrangements, Li interstitials may induce enhanced local "rattling" motion, which can disrupt correlated Li migration and ultimately reduce ionic conductivity.

Linear relation between Li diffusivity and ionic conductivity

In this work, we compared the calculated diffusivity with the experimental ionic conductivity on the grounds that they are linearly proportional to each other, according to Nernst-Einstein relation. Specifically, the ionic conductivity σ can be expressed in terms of the diffusivity D through the Nernst–Einstein relation as follows.

$$\sigma = \frac{nq^2}{k_B T} D \cdot H$$

Here, n is the number of mobile ions per unit volume, q is the ionic charge, k_B is the Boltzmann constant, and T is the absolute temperature. The factor H represents the Haven ratio (or correlation factor), which accounts for the correlation effects between ionic motions. When $H = 1$, each ion diffuses independently, whereas smaller values indicate that multiple ions move in a correlated manner during diffusion. In this study, we assume that the H values are comparable for both the X-doped and LiX-doped LPS model structures. Therefore, the ionic conductivity and diffusivity can be compared based on their linear proportionality. The rationale for this assumption is described below.

The Haven ratio, $H_R = D_{\text{charge}}/D_{\text{self}}$, is defined as the ratio between the charge diffusivity (D_{charge}), which represents how much the ionic motion contributes to the net charge transport, and the self-diffusivity (D_{self}), which reflects how far individual ions move. In other words, it compares the average displacement of each Li ion in MD simulations with the extent to which their collective motion contributes to actual ionic conduction. If all ions diffuse independently and randomly, the two diffusivities become similar and H_R approaches unity ($H_R \approx 1$). However, in real solid electrolytes, correlated collective behaviors such as back-correlation, concerted hopping, and cooperative motion are often present, which reduce the net charge transport relative to the individual ionic displacement. Therefore, the Haven ratio is not merely a measure of ionic mobility but also a statistical indicator reflecting the degree of correlation among ionic motions, providing a physical measure of the effect of cooperative ion dynamics.

Even without explicitly calculating the Haven ratio, its magnitude can be qualitatively inferred using the correlation function $C(t)$, which reflects the degree of correlation in ionic motion [6]:

$$C(t) = \frac{\langle |\sum_i \Delta r_i(t)|^2 \rangle}{\sum_i \langle |\Delta r_i(t)|^2 \rangle}$$

In this expression, the denominator represents the self-diffusion component, corresponding to the sum of the mean squared displacements (MSD) of individual ions, while the numerator

represents the collective charge transport component expressed as the squared magnitude of the summed displacement vectors. Therefore, the value of $C(t)$ in the long-time regime quantitatively indicates whether ions move independently or exhibit correlated (cooperative) behavior. In particular, the long-time plateau or slope of $C(t)$ is directly related to the correlation effects that determine the Haven ratio, and thus can be used as an indicator for comparing the relative magnitude of H_R between different systems.

For this reason, in this study we calculated $C(t)$ for the X- and LiX-doped LPS models obtained from molecular dynamics simulations and analyzed the collective ion-transport characteristics and the degree of correlation in each system by comparing the overall trends of the $C(t)$ curves (see Figure S13). The results showed that X-doped LPS has similar $C(t)$ values in the long-time regime regardless of the type of halogen dopants, which is also the case for LiX-doped LPS. Considering that the $C(t)$ curves directly represent the Haven ratio H, the H values are considered to be comparable for both the X-doped and LiX-doped LPS model structures and thus, the ionic conductivity and diffusivity can be compared based on their linear proportionality.

Methods

Geometry optimization of atomic structures. To provide reliable description of the Li diffusion kinetics in $Li_7P_3S_{11}$ (LPS) solid electrolytes (SEs), all model atomic structures used in this study were optimized using density functional theory (DFT) calculations prior to carrying out molecular dynamic simulations. All DFT calculations were conducted using the Vienna Ab initio Simulation Package (VASP) code [7]. Interactions between core and valence electrons were described using the projector augmented wave (PAW) method [8]. The revised Perdew–Burke–Ernzerhof Generalised Gradient Approximation (GGA) functional (PBEsol) [9] was employed to deal with the exchange-correlation potential, as it has accurately reproduced lattice parameters and lattice dynamics in solid systems while maintaining a relatively low

computational cost [10]. The electron configurations of Li (1s2), Ge ($4s^24p^2$), P ($3s^23p^3$), S ($3s^23p^4$), F ($2s^22p^5$), Cl ($3s^23p^5$), Br ($4s^24p^5$), and I ($5s^25p^5$) were treated as the valence electrons. Convergence to plane wave energy was checked, with a cut-off of 550 eV found to be sufficient to converge the total energy to within 0.01 eV $atom^{-1}$. Brillouin zones for all compounds were sampled such that the k-points were converged in an accuracy of the total energy in 0.001 eV $atom^{-1}$. All calculations were deemed to be converged when the forces on all atoms were less than 0.01 eV $Å^{-1}$.

Construction of model atomic structures. To generate large-scale atomic structures for molecular dynamic simulations, the pristine LPS crystal structure ($P\bar{1}$) with 42 atoms was first retrieved from Materials Project [11] and optimized using the PBEsol method (see Geometry optimization of atomic structures). To construct X- and LiX-doped LPS structures, the most preferential halogen dopant site was searched by substituting halogen element on 11 crystallographically distinct sulfur sites (see Fig. S1 in Supporting Information). For X-doped LPS, Li^+ ion nearby halogen dopant was removed to compensate for the charge difference between the halogen (X^-) and the host sulfur (S^{2-}) ion. For LiX-doped LPS, Li interstitial sites were determined in a non-arbitrary manner by systematically identifying geometrically accessible empty spaces intrinsic to the crystal structure, into which Li^+ ions were subsequently inserted. Candidate interstitial sites were generated using a Voronoi-partition–based interstitial search algorithm implemented in the pymatgen interstitial generator [12]. These sites were defined as regions of locally minimized atomic density that are maximally distant from surrounding atoms. The Voronoi-derived candidate positions correspond to spatial regions where Coulombic and Pauli repulsions associated with additional cation insertion are relatively small, and thus represent structurally accessible empty spaces capable of accommodating interstitial species. This procedure enables the identification of potential interstitial coordinates solely based on the geometric characteristics of the crystal structure, prior to electronic structure calculations.

Because the Voronoi-generated interstitial candidates are initially confined to the asymmetric unit, space-group symmetry operations were applied to generate all symmetry-equivalent empty spaces throughout the crystal. Candidate sites separated by less than 0.1 Å were

considered equivalent and merged accordingly to remove redundant or overlapping positions. From the resulting set of distinct interstitial sites, those minimizing direct electrostatic interactions with doped halogen anions were selected for Li interstitial insertion. All resulting structures were subsequently fully relaxed using density functional theory (DFT) geometry optimizations to achieve complete structural stabilization.

Machine-learning-based molecular dynamic (ML-MD) simulations. Molecular dynamics simulations with graph neural networks with three-body interactions (M3GNet) [13] were carried out to describe the complex Li diffusion kinetics including cooperative hopping and paddle-wheel dynamics. To this end, the cation-substituted model structures of X- and LiX-doped LPS generated from Construction of model atomic structures were fully optimized using the PBEsol method. The optimized structures were then expanded into [6 × 3 × 2] supercells (~1000 atoms) to provide a more comprehensive and statistically meaningful data on the complex Li-ion transport mechanisms. Prior to simulating the diffusion process of Li, equilibration simulations were performed at 300 K for 3 ps to stabilize the model structures in the NVT ensemble, followed by the lattice parameter optimization to release the local internal stresses. The model structures were then heated to 300, 325, 350, 375, and 400 K using Berendsen's thermostat [14] under NVT ensemble. The Verlet algorithm was used to solve classical equations of motion for 20 ps with a time step of 1.0 fs for the model structures. To further demonstrate the convergence of diffusivity in a longer time regime, we performed a similar analysis on X-doped LPS model structures under prolonged time of 60 ps (see Figure S16). The diffusivity trends and energy barrier values are more or less similar to those calculated in a 20 ps regime, which indicates that a 20 ps simulation time is sufficient to reliably capture the relative changes in Li-ion transport behavior induced by halogen doping. To further validate the accuracy of ML-MD in describing atomic structures of LPS, X-, and LiX-doped LPS, we evaluated the structural difference between ML-MD-driven structures and DFT-optimized structures. This

was achieved by extracting the model structures during ML-MD and subsequently optimizing them using two different methods of M3GNet interatomic potential (IAP) and DFT calculations, followed by comparing the volume and bond lengths of optimized model structures. The parity plot reveals that the calculation results of the M3GNet IAP for the LPS materials before and after doping are more or less close to the ideal regression line (see Figure S11). These results demonstrate that the M3GNet IAP used in this study can approximate interatomic interactions close to DFT.

The recorded atom positions represent the movements of tetrahedral clusters and Li ions at a given temperature and thus, can be used to estimate the degree of cooperative hopping and the diffusivity of Li and dopants. To estimate the degree of cooperative hopping occurred in the model structures, we counted the hopping frequency of Li during MD simulations and classified them by the number of simultaneously hopping Li atoms. This was done in three steps: 1) collect the atomic indices and positions of Li on a time interval of 1.0 ps. 2) if a Li atom moved more than 2.6 Å during the given time interval of 1.0 ps, count it as a "hopped" Li atom. 3) if two (or three) hopped Li atoms are close to each other within 4 Å before and after hopping, count them as double (or triple) hopping. The cooperative hopping behaviors were further examined by using the statistical mean of van Hove correlation function $G_d(r,t)$ [15] as implemented in the open-source MD package GROMACS [16]. The $G_d(r,t)$ value represents the probability that a particle moves a distance of r in time t, which is defined as

$$Gd(r,t) = \frac{1}{N} < \sum_{i \neq j}^{N} \delta[r + rj(t=0) - ri(t)] >$$

where δ, $r_j(t=0)$, and $r_i(t)$ are the Dirac delta function, a j^{th} ion at t = 0 ps, and another ion at distance of ri at time t, respectively.

To estimate the diffusivity of Li and dopants in the model structures, the mean square displacement and associated diffusivity values were estimated by using Bayesian linear regression via Markov-chain Monte Carlo sampling of linear models as implemented in KINISI [17].

Fraction of structural transitions in substructure. To quantify the transitions of PS_x-type polyhedral units (e.g., PS_4^{3-} and $P_2S_7^{4-}$) during molecular dynamics (MD) simulations, a Python-based analysis tool was employed. This tool identifies structural motifs of the form MX_x (M: central element such as P or Ge; X: corner element such as S or Cl) by searching local clusters in which the bond lengths between M and X atoms are less than a cutoff distance. Here, the cutoff distance was determined by calculating the radial distribution functions (RDF) of P–X bonds within X-doped LPS (Figure S6). In general, the nearest-neighbor distances extracted from the partial RDFs provide reliable estimates of the average atomic bond lengths, consistent with well-defined chemical bonding in the crystalline lattice [18]. In addition, bond breakage was determined based on whether the interatomic distance exceeded the second nearest-neighbor distance. For this reason, the bond-breaking cutoff for each atomic pair was defined as the first minimum between the first and second coordination shells in the corresponding partial RDFs. When examining the calculated partial RDF plots in Figure S6, all P–X pairs (i.e., P–F, P–Cl, P–Br, and P–I) in X-doped LPS show first peaks near 2 Å and second peaks near 4 Å. Therefore, a cutoff distance of 3.0 Å was used to define bond breaking throughout this work. Based on the predefined cutoff distance of 3.0 Å, at each timestep during MD simulations, the python script classifies atoms into polyhedral clusters with consisting atoms being bonded to each other with an interatomic distance less than 3.0 Å, followed by categorizing them into structural formulas (e.g., MX_4, M_2X_7) depending on the number of center and corner atoms in each cluster. The structural evolution of these clusters were then

quantified by tracking their atomic indices and type of polyhedral on a time interval of 1.0 ps. For example, if a phosphorus atom (atomic index P1) belongs to a PS_4 motif (see Figure S15 for the cutoff distance of P–S bonds) at 2.0 ps but is identified as part of a P_2S_7 motif at 3.0 ps, this event is counted as one PS_x transition. After this event, the number of PS_4 motifs decreases by one while the number of P_2S_7 motifs increases by one. This enables the quantification of (i) the fractional population of each structural motif over time and (ii) the number of structural transitions.

References

1 B. Lee, K. J. Jun, B. Ouyang and G. Ceder, *Chemistry of Materials*, 2023, **35**, 891–899.

2 B. Zhang, Z. Lin, H. Dong, L. W. Wang and F. Pan, *J. Mater. Chem. A Mater.*, 2020, **8**, 342–348.

3 E. Madelung, *Phys. Z*, 1918, **19**, 524–533.

4 D. O. Scanlon, C. W. Dunnill, J. Buckeridge, S. A. Shevlin, A. J. Logsdail, S. M. Woodley, C. R. A. Catlow, M. J. Powell, R. G. Palgrave, I. P. Parkin, G. W. Watson, T. W. Keal, P. Sherwood, A. Walsh and A. A. Sokol, *Nat. Mater.*, 2013, **12**, 798–801.

5 J. Buckeridge, K. T. Butler, C. R. A. Catlow, A. J. Logsdail, D. O. Scanlon, S. A. Shevlin, S. M. Woodley, A. A. Sokol and A. Walsh, *Chemistry of Materials*, 2015, **27**, 3844–3851.

6 N. M. Vargas-Barbosa and B. Roling, *ChemElectroChem*, 2020, **7**, 367–385.

7 G. Kresse and J. Hafner, *Ab. initio molecular dynamics for liquid metals*, vol. 47.

8 G. Kresse and D. Joubert, *From ultrasoft pseudopotentials to the projector augmented-wave method*, .

9 J. P. Perdew, A. Ruzsinszky, G. I. Csonka, O. A. Vydrov, G. E. Scuseria, L. A. Constantin, X. Zhou and K. Burke, DOI:10.1103/PhysRevLett.100.136406.

10 J. M. Skelton, D. Tiana, S. C. Parker, A. Togo, I. Tanaka and A. Walsh, *Journal of Chemical Physics*, DOI:10.1063/1.4928058.

11 A. Jain, S. P. Ong, G. Hautier, W. Chen, W. D. Richards, S. Dacek, S. Cholia, D. Gunter, D. Skinner, G. Ceder and K. A. Persson, *American Institute of Physics Inc.*, 2013, preprint, DOI: 10.1063/1.4812323.

12 S. P. Ong, W. D. Richards, A. Jain, G. Hautier, M. Kocher, S. Cholia, D. Gunter, V. L. Chevrier, K. A. Persson and G. Ceder, *Comput. Mater. Sci.*, 2013, **68**, 314–319.

13 C. Chen and S. P. Ong, DOI:10.1038/s43588-022-00349-3.

14 A. S. Lemak and N. K. Balabaev, *Mol. Simul.*, 1994, **13**, 177–187.

15 L. Van Hove, *Correlations in Space and Time and Born Approximation Scattering in Systems of Interacting Particles*, 1954.

16 D. Van Der Spoel, E. Lindahl, B. Hess, G. Groenhof, A. E. Mark and H. J. C. Berendsen, 2005, preprint, DOI: 10.1002/jcc.20291.

17 A. R. McCluskey, A. G. Squires, J. Dunn, S. W. Coles and B. J. Morgan, *J. Open Source Softw.*, 2024, **9**, 5984.

18 B. H. Toby and T. Egami, *Acta Crystallographica Section A*, 1992, **48**, 336–346.